Materials Science & Engineering A 837 (2022) 142727

Contents lists available at ScienceDirect

Materials Science & Engineering A

journal homepage: www.elsevier.com/locate/msea

Twin density gradient induces enhanced yield strength-and-ductility synergy in a S31254 super austenitic stainless steel

Ting-Ting Chen [a,b], Jing Wang [b], Yi Zhang [a], Ping Jiang [b], Fu-Ping Yuan [b,c], Pei-De Han [a,**], Xiao-Lei Wu [b,c,*]

[a] School of Material Science and Engineering, Taiyuan University of Technology, Taiyuan, 030024, China
[b] State Key Laboratory of Nonlinear Mechanics, Institute of Mechanics, Chinese Academy of Sciences, Beijing, 100190, China
[c] School of Engineering Science, University of Chinese Academy of Sciences, Beijing, 100049, China

ARTICLE INFO

Keywords:
Gradient structure
Deformation twin
Strain hardening
Hetero-deformation

ABSTRACT

Gradient structure (GS), as a typical heterostructure, is arousing great interest for an improved synergy between the strength and ductility which are mutually conflicting. Recently, a novel design of GS is proposed by taking the density of twins in grains, instead of common grain size, as a gradient variable, showing the key role in strain hardening by the nano-scale twin boundaries. Following this idea, here, a deformation twin-density GS was produced by means of the technique of surface mechanical attrition treatment in a S31254 super austenitic stainless steel. To be specific, the GS consisted of a central coarse-grained (CG) core, with two sides sandwiched by the gradient-structured layer (GL), where the density of deformation twins appears gradient in grains along the depth towards the CG core. The tensile tests show that as compared to CG counterpart, yield strength in GS increases 80% to 0.5 GPa, along with comparable ductility of 36%. The interrupted tensile tests show the presence of mechanical hysteresis loops during each unload-reload cycle, indicative of the generation of hetero-deformation-induced (HDI) stress during tensile deformation. Furthermore, both the HDI stress and HDI strain hardening account for a large proportion of global flow stress and forest hardening. The deformation twins and their evolutions, with the emphasis on their interaction with the dislocations, are investigated in detail by means of EBSD and TEM observations to correlate the mechanical properties. The present results shed light on the crucial role of deformation twins in the twin-density gradient for the synergistic enhancement of both strength and ductility.

1. Introduction

Both yield strength and ductility (i.e., uniform elongation under tensile loading) are two important mechanical properties in metals and alloys for engineering application [1,2]. However, strength and ductility are usually conflicting mutually with an insurmountable trade-off [3–5]. Namely, an increase in strength by either grain refinement or cold work is always accompanied at the loss of ductility [5–7]. The reason behind it is the diminishing strain hardening by traditional dislocation plasticity [1,5,6], which cannot catch up with the increase in flow stress during plastic deformation according to the Considère criterion. To enhance the balance between strength and ductility, the heterostructure-oriented strategy is advocated recently [8–11]. By comparison with the conventional homogeneous microstructure, the heterostructure (HS) features, to be brief, the combination of soft and strong grains of various flow behaviors such that the hetero-deformation induced (HDI) stress will be produced at the hetero-boundaries between soft and strong grains in response to straining [9]. This HDI stress facilitates an extra HDI-hardening not only to reinforce global strain hardenability but also to provide compatible deformation at the hetero-boundaries, otherwise plastic instability will occur at first. The HDI hardening is ascribed from the geometrically-necessary dislocations (GNDs) to accommodate strain gradient as a result of the locally non-uniform deformation to occur at the hetero-boundaries [9,10]. The GNDs, usually in the initial form of dislocation pile-up [12], are the origin of HDI stresses. So far, the heterostructures of varying kinds are designed, aiming at the synergistic effect for strain hardening, typical heterostructures including the gradient structure [13,14], lamellar structure [8], multi-level grain

* Corresponding author. State Key Laboratory of Nonlinear Mechanics, Institute of Mechanics, Chinese Academy of Sciences, Beijing, 100190, China.
** Corresponding author.
E-mail addresses: hanpeide@tyut.edu.cn (P.-D. Han), xlwu@imech.ac.cn (X.-L. Wu).

https://doi.org/10.1016/j.msea.2022.142727
Received 7 November 2021; Received in revised form 17 January 2022; Accepted 22 January 2022
Available online 24 January 2022

[15], and core-shell structure [16] etc., all typical of the hetero-boundaries of high density for HDI hardening to take effect during tensile deformation [9,17,18].

The gradient structure (GS) is shown to be able to effectively enhance yield strength and ductility balance [2,13,14,17,18]. The earlier GS is focused on the grain size gradient [13,14,18], typical of the *trans*-scale grain hierarchy. This GS consists of the nanograins/nanostructures (NS) in the surface layer and CG counterpart in the center layer, in-between with a continuous increase in grain size. The GS demonstrates a synergistic effect due to the additional HDI hardening [19,20]. However, this kind of GS still suffers from poor strain hardening particularly in the NS layer where the dislocations of high density generated during the fabrication of GS play a strong constraint in the further storage of dislocations to harden these grains during subsequent tensile deformation [13,14].

Recently, an ingenious strategy has been proposed of a pioneer GS design for extraordinary strain hardening with the density of twin boundary of nano-twins (NT) acting as the gradient variable [21]. The distinctive advantage in this NT-density GS lies in the superior strength and ductility synergy especially at an enhanced yield strength [21]. This is ascribed to the crucial effect of nano-scale twin boundaries (TBs). On one hand, TBs facilitate strain hardening in terms of strong interactions with gliding dislocations especially when spacing of TBs is at nano-scale [22,23]. On the other hand, the nano-scale TBs are mechanically stable to play a similar role to grain boundaries to refine the grains [2,21], which leads to an extra strengthening [21]. Note that these NTs are either growth or annealing ones usually formed during electrodeposition and annealing [21,22].

The popular plastic-deformation-based technique is also an appropriate method to fabricate the NT-density GS [24–27], typical methods including surface mechanical attrition treatment (SMAT) [28], surface mechanical grinding [29], surface sliding [30], and surface rotation [31] etc. As for all these techniques, the feature in common is to exert accumulative plastic deformation on the surface of bulk specimens. The applied strains, along with strain rate, are gradient-distributed along the depth in the surface layer, which makes the microstructure refine to form the gradient [28]. For a metal/alloy of low stacking fault energy (SFE), deformation twinning is the dominant response to accommodate plastic deformation and resultantly, the density of deformation twins (DTs) will be produced in the form of a gradient. The closer distance to the top surface, the high density of DTs will be. Yet, it is worthy to note that in this DT-density gradient, the grains are full of the dislocations of high density.

The super austenitic stainless steels (SASS) have recently attracted great attention for the superior combination of mechanical properties and corrosion resistance. The typical SASS is S31254 [32,33], with the additions of alloying elements, e.g., molybdenum and nickel etc., by comparison to the traditional austenitic stainless steels. Unfortunately, the glaring drawback is the low yield strength of only 280 MPa in this S31254 SASS. In this regard, the GS is proposed as a preferred strategy to strengthen and strain harden the S31254 SASS without compromising the corrosion resistance. In the present investigation, the DT-density GS was fabricated by using the SMAT processing. Both the tensile property and microstructural evolution are experimentally investigated to show an enhanced combination between strength and ductility in GS, along with an enhanced strength.

2. Experimental procedures

2.1. Materials and SMAT processing

The thin plate of 1.3 mm thick was used in a S31254 SASS for the present investigation. The chemical composition (weight percent) was 0.009C, 19.79Cr, 17.88Ni, 0.81Mn, 0.75Cu, 5.83Mo, 0.63Si, 0.21 N, 0.01Nb, 0.01Al, balance Fe. The initial coarse-grained (CG) microstructure was the face-centered-cubic (fcc)-structured single phase after high temperature annealing at 1497 K for 2 h.

The GS specimens were fabricated in the annealed CG plate by using the SMAT technique [28]. During SMAT processing, the steel shots were accelerated in a closed container by a high-power ultrasonic device operated at high system frequency (20 kHz). This caused the surface of plate specimen in the container to be randomly peened at extremely high strain rates. In other words, the layer was severely deformed from the surface to certain depth. In consideration of both the deformed layer depth and surface roughness during SMAT processing, the processing parameters were determined after a series of experiments as the shots of 2 mm in diameter and the processing period of 45 min for each side of the plate sample. Finally, the GS specimen was obtained with the gradient layers (GLs) on both surfaces sandwiching the central CG layer.

2.2. Mechanical property tests

All tensile specimens were dog-bone shaped, with a gauge cross-section of 4×1.3 mm^2 and 18 mm length. Tensile specimens were cut from the SMAT-processed plate with the longitudinal axis along original rolling direction. The tensile specimens of varying thickness were also prepared in GS specimens to test the tensile properties at the specific depth. These thin specimens were obtained by polishing away the initial GS specimen from one side, leaving behind the specimen of desired thickness for tensile testing.

The quasi-static uniaxial tensile tests were carried out at a strain rate of 5×10^{-4} s^{-1} and at ambient temperature in an MTS Landmark testing machine. The extensometer was attached on the gauge section of tensile specimen to measure applied strain during tensile deformation. The interrupted load-unload- reload (LUR) tensile testing was performed under the similar tensile conditions to the monotonic one. During LUR testing, once straining to certain value at strain rate of 5×10^{-4} s^{-1}, the specimen was unloaded by the stress-control mode to 20 N, followed by reloading at a strain rate of 5×10^{-4} s^{-1} to the next unload strain. For reproducibility, both monotonic and LUR tensile tests were carried out at least three times on average. The method to calculate HDI stress (σ_{HDI}) can be found in Ref. [19] in which the measured back stress is actually σ_{HDI}.

The Vickers micro-hardness (H_V) were measured on the cross-section of GS specimen before and after tensile testing. Each testing was maintained with a dwelling time of 15 s under a loading of 25 g.

2.3. Microstructural characterization

The microstructure was characterized by using an electron backscattered diffraction (EBSD) attached on a Zeiss Gemini SEM 300 scanning electron microscope (SEM). Before EBSD observation, the cross-sections of GS samples were mechanically polished. The measurements by X-ray diffraction (XRD) were performed to characterize the phase structure by using a Rigaku Smart lab X-ray diffractometer with Cu Kα radiation. The microstructures and specifically, deformation twins and dislocations were also investigated in a FEI TECNAI G2 20 S transmission electron microscope (TEM) operated at a voltage of 200 kV. TEM specimens were cut from the gauge section of tensile samples. Thin foils for TEM observations were mechanically polished to ~50 μm thick, then punched to disks 3 mm in diameter. Perforation by twin-jet electropolishing was carried out using a solution of 8% perchloric acid and 92% ethanol at −28 °C and 38V.

3. Results

3.1. As-processed microstructure

Fig. 1a is the EBSD inverse pole figure (IPF), showing the homogeneous coarse-grained (CG) microstructure after recrystallization annealing. The statistic average grain size is 200 μm. Fig. 1b shows the distribution of Vickers micro-hardness (H_V) values along the depth of

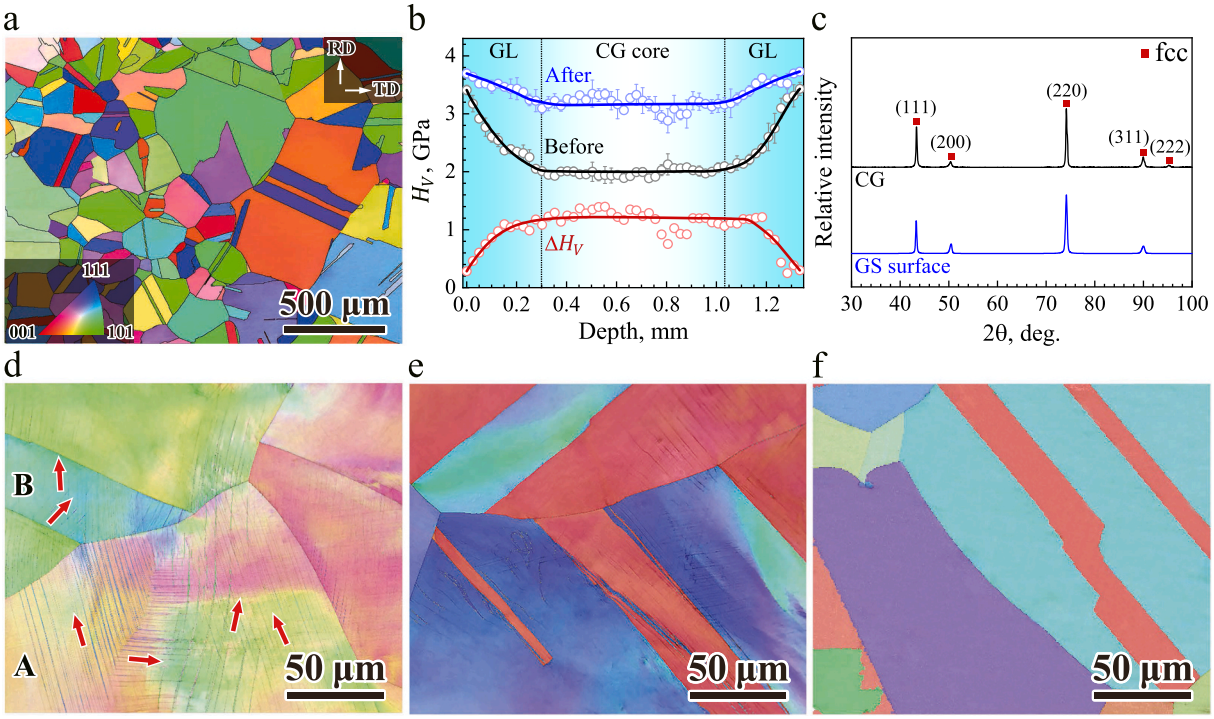

Fig. 1. Microstructural characterization of gradient-structured (GS) specimen. (a) EBSD IPF of as-annealed coarse-grains (CG). (b) Distribution of H_V values across the depth of GS specimen before and after tensile testing. GL: gradient-structured layer. (c) XRD spectra of CG and treated top surface of GS specimen. (d)–(f) Superimposed IPF and IQ map at the depth of ~50 and 100 μm in GL and of ~600 μm in CG core. Arrows in (d): deformation twins in grain A and twin B.

cross-section of the GS specimen before and after tensile deformation. H_V shows an obvious gradient of ~300 μm thick on both sides, which are considered as the gradient layer (GL). In total, 45% of the total thickness of the GS specimen is accounted for by the two gradient layers. By comparison, the central CG layer shows a smooth H_V. The maximum H_V value reaches 3.4 GPa at the treated surface, which is much larger than 2 GPa in the central CG core. Both the CG layer and GL are the fcc single phase, as evidenced by the XRD spectra as shown in Fig. 1c. This indicates that no phase transformation happens during the SMAT processing.

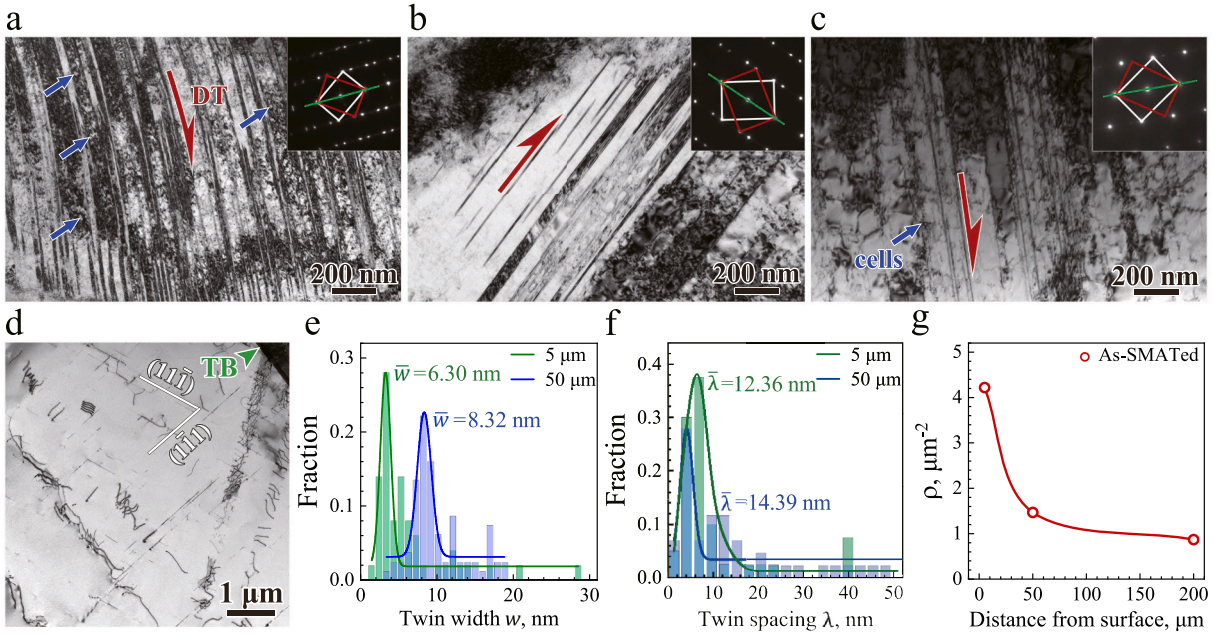

Fig. 2. Bright-field TEM micrographs showing initial microstructures at various depths in the GS. (a)–(c) Deformation twins at the depth of ~5, 50 and, 200 μm deep, respectively, below the treated surface. Inset in each map: the corresponding selected area electron diffraction (SAED) pattern of twin, all with the [011] zone axis. Red arrows: twin boundaries. Blue arrows: dislocation tangles in (a, b) and cells in (c). (d) Slip micro-bands in CG core. Green arrow: an annealing twin boundary. (e)–(f) Statistical distribution of both width w and spacing λ of nanotwins at different depths. (g) Statistical density of nanotwins at different depth of as-SMATed sample.

Fig. 1d–f are a set of EBSD images by superimposing image quality (IQ) map on inverse pole figure (IPF) taken at varying depths of GS specimen. Fig. 1d shows DTs of high density at ~50 μm deep. Interestingly, at least four successively activated twin systems are visible in the grain labeled by A, see red arrows parallel to TB. DTs are also observed in a thick annealing twin, labeled by B. Some DTs are bended to accommodate large local strains during SMAT. Importantly, the density of DTs decreases towards the interior of GL, see Fig. 1e taken at ~100 μm deep, and become hardly visible in the CG layer, see Fig. 1f at ~600 μm deep. Accordingly, the DT-density gradient, instead of the conventional grain-size one [13,14], is induced in the GS. This is due to applied high strain rates during SMAT which facilitates deformation twinning to happen preferentially in this SASS of low SFE. Further, EBSD observations do not show any sign of grain refinement to happen in GL.

The DTs are further studied at different depths in GL by TEM observations. Fig. 2a shows a bundle of DTs of high density at the depth of 5 μm, much near the treated surface. These DTs are much thin, along with dislocation tangles. The statistic average twin width ($\overline{w}$) and spacing ($\overline{\lambda}$) is 6.3 nm and 12.4 nm, respectively, along with the number density (ρ) of 4.22 μm^{-2}, see Fig. 2e, f and 2g. These twin lamellae and dislocations of high density is the reason of high H_V in the treated surface. As the depth increases to 50 and 200 μm respectively, the density of NTs and dislocations decreases, see Fig. 2b and c. Accordingly, $\overline{w}$ and $\overline{\lambda}$ for DTs slightly increase, along with a decreased ρ, see Fig. 2e, f and 2g. By comparison, the slip micro-bands (MBs) are the dominant substructure to accommodate plastic deformation in the CG layer at ~600 μm deep, see Fig. 2d; while DTs are absent. These MBs nucleates and glides on the {111} planes [26], with the planar arrays dislocation in the interiors.

3.2. Tensile property

Fig. 3a is a set of tensile engineering stress-strain ($\sigma_e - \varepsilon_e$) curves in various specimens. The GS specimen exhibits the combination of yield strength (σ_y) of 0.5 GPa and ductility (ε_u) of 36%. σ_y in GS is almost twice that in CG, only with a slight drop in ε_u. For other thin samples of 0.14 and 0.32 mm thick (keeping one treated surface, labeled as $GL_{0.14}$ and $GL_{0.32}$, respectively), the thinner sample, the higher σ_y and accordingly, the less ε_u will be. σ_y is as high as 1.75 GPa in the free-standing $GL_{0.04}$ of 40 μm thick. Fig. 3b shows the strain hardening rate ($\Theta = \frac{\partial\sigma}{\partial\varepsilon}$) versus true strain ($\varepsilon_T$) curves. All curves can be approximately divided to three stages, except for $GL_{0.04}$. Θ fall dawn steeply at first, followed by the moderate rise and final slow drop. The steep drop of Θ in standalone $GL_{0.04}$ is in contrast to that in GS where $GL_{0.04}$ is attached. This indicates a special mechanism in GS to work which changes plastic deformation in $GL_{0.04}$.

The HDI stress and HDI strain hardening were investigated by conducting LUR tensile tests. The mechanical hysteresis loops appear during each unload-reload cycle in both GS and CG. Fig. 3c shows loops at two typical unload strains. This indicates the onset of reverse plastic flows upon unload even though the applied stress is still in tension [8,15]. The presence of hysteresis loops is an unambiguous sign to indicate that the HDI stress (σ_{HDI}) begins to take effect [9,10,19]. The residual plastic strain (ε_{rp}), defined as loop width [19], is used to characterize the HDI effect. Interestingly, ε_{rp} in GS is larger than that in CG at strain less than ~18%, see Fig. 3d, beyond which Θ begins to drop, see Fig. 3b. HDI stress (σ_{HDI}) is can be estimated as [19],

$$\sigma_{HDI} = \frac{\sigma_r + \sigma_u}{2}$$

where σ_u and σ_r are the unloading yield stress and the reloading yield stress from the hysteresis respectively. The $\sigma_{HDI} - \varepsilon_T$ curve was then fitted. The hardening rate of HDI stress was obtained by taking derivative of the fitting curve, i.e., $\Theta = \frac{\partial\sigma_{HDI}}{\partial\varepsilon_T}$. The upper panel in Fig. 3e shows the proportion of σ_{HDI} to σ_T in both CG and GS, while the lower panel is that of hardening rate by σ_{HDI} (Θ_{HDI}) to Θ_T. It is visible that both $\sigma_{HDI}/\sigma_{flow}$ and $\Theta_{HDI}/\Theta_{flow}$ in GS almost keep a slight decrease (merely a little bit higher) as compared to those in CG when strain is less than ~18%. However, σ_y in GS almost doubles that in CG, only with a little bit decrease in ductility. Fig. 3f shows the (σ_y ε_u) combination in all samples. If roughly considering only a weak gradient of twin density in thin $GL_{0.14}$, it is seen that GS enhances the (σ_y ε_u) balance indeed.

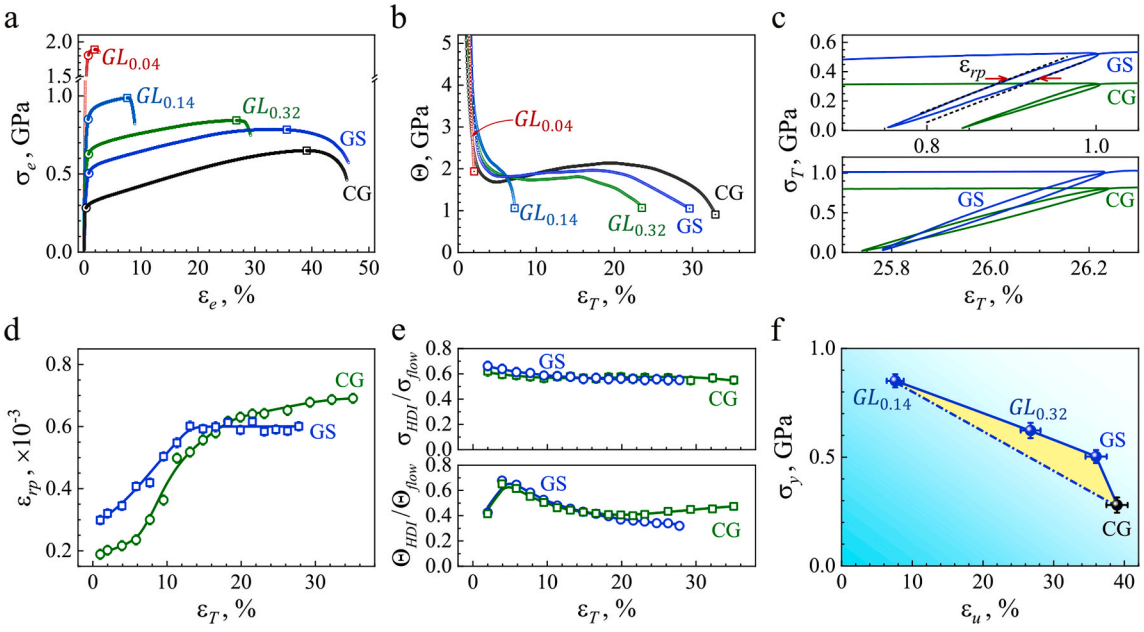

Fig. 3. Tensile mechanical behavior of GS S31254. (a) $\sigma_e - \varepsilon_e$ curves. CG: coarse grain. GS: the gradient structure. GL_{no}: gradient layer; subscript (no): sample thickness in mm. (b) $\Theta - \varepsilon_T$ curves. (c) Mechanical hysteresis loops in GS and CG at unloading strain of 1% (upper panel) and 26.2% (lower panel). (d) $\varepsilon_{rp} - \varepsilon_T$ curves in GS and CG. (e) $\sigma_{HDI}/\sigma_{flow} - \varepsilon_T$ (upper panel) and $\Theta_{HDI}/\Theta_{flow} - \varepsilon_T$ (lower panel) curves in GS and CG. (f) (σ_y, ε_u) balance.

3.3. Microstructural evolution after tensile testing

The unique effect of TBs in GS and CG is investigated during tensile deformation. The kernel average misorientation (KAM) is for displaying small orientation changes on the map. Thus, the KAM value can qualitatively reflect the homogenization degree of plastic deformation, highlighting regions of higher deformation or higher defect density. The change of KAM values directly reflects the density of GNDs to accommodate strain gradient near GBs and TBs [34,35]. Usually, the larger KAM values, the higher density of GNDs will be. Fig. 4a–c are the EBSD KAM-value images at ~50 and 200 μm deep, respectively, in GL of GS specimen and in CG core, all before tensile deformation. Fig. 4d–f shows the KAM images at the same depths observed after tensile deformation. The scanning step size of Fig. 4a–f is 0.3 μm, while that of insets in Fig. 4d–f is 0.05 μm. The statistic KAM value distribution near GB and TB before tensile deformation is shown in Fig. 4g, along with the average KAM value ($\overline{K}$). It is visible that $\overline{K}$ of 0.8° near GB in GL (upper panel) is close to that of 0.6° near TB (lower panel) at 50 μm deep. And, $\overline{K}$ near GB in GL (blue curve, upper panel) is much larger than that of 0.2° in CG (orange curve). Fig. 4h is the corresponding analysis after tensile deformation. Several key features are noted. First, for GL, two $\overline{K}$ near GB (upper panel) and TB (lower panel) increase, respectively, from 0.8° to 1.4° and from 0.6° to 1.0°. Second, for CG layer, $\overline{K}$ near GB increase from 0.2° to 1.1°, while $\overline{K}$ near TB is 0.7° for newly-formed deformation twins during tensile deformation. Finally, $\overline{K}$ near both GB (upper panel, Fig. 4h) and TB (lower panel) is always higher in GL than that in CG, together with an obvious increase in the proportion of large KAM values. The detailed analysis is further made to reveal the key role of twin boundaries, as illustrated in Fig. 4i, which shows the distribution of KAM values across the twin plate, pointed by red arrow, see close-up view in inset of Fig. 4d. Of interesting note is the larger KAM values near twin boundaries than those inside twins. This means the key effect of twin boundaries for an increased KAM values probably due to the blockage and interaction with the gliding dislocations during plastic deformation [36,37]. Fig. 4j is the statistic grain boundary misorientation in GL at 50 μm deep before and after tensile deformation. Meanwhile, the frequency is almost unchangeable at least in GL of 50 μm deep before and after

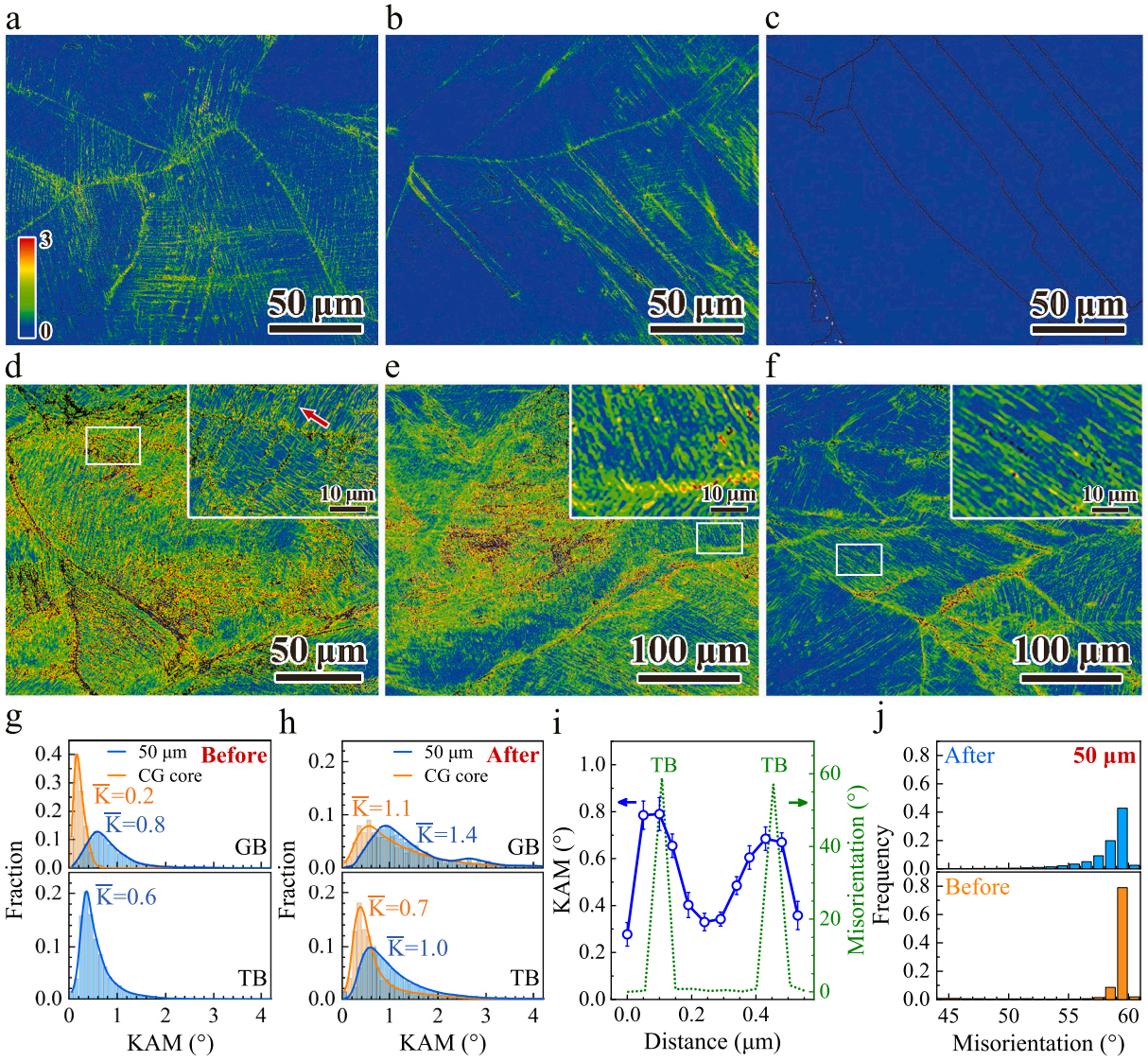

Fig. 4. KAM evolution of GS before and after tensile testing. (a)–(c) KAM map at depth of ~50 and 200 μm and at CG core before tensile testing. (d)–(f) KAM map at depth of ~50 and 200 μm and at CG core after tensile testing. Inset in each map: close-up view taken from white rectangle. Red arrow of inset in Fig. 4d: deformation twin. (g) and (h) Statistical KAM distribution near boundaries before and after tensile testing at depth of ~50 μm and at CG core respectively. (i) KAM values across the twin pointed by red arrow in Fig. 4d at depth of ~50 μm after tensile testing. (j) Statistical frequency of TBs at depth of ~50 μm before and after tensile, respectively.

deformation by analyzing a large number of EBSD and TEM images. In other words, no twinning happens during tensile deformation. This indicates that the deformation twins, even with the entangled high density dislocations already, may still plastically deform to large strains in GS. Such a high percentage of TBs proves again important effect of TBs on strain hardening, which is even more efficient than that by GBs.

Fig. 5a and b are TEM images taken at ~170 and 330 μm deep in GL after tensile deformation. The multiple DTs are visible, together with the dislocation tangles inside DTs.

4. Discussion

The present DT-density GS almost doubles in yield strength by comparison to the CG, along with comparable ductility (Fig. 3a). GS exhibits an anti-banana-like strength and ductility relationship by contrast to the homogeneous CG counterpart (Fig. 3f). Further, for any layer in GS, e.g., $GL_{0.14}$, ductility is only 8% when testing standalone, while increases to 36% only if attached on the surface of GS. The marked feature is therefore the increase in ductility at the similar strength in GS. This is, actually, a shared characteristics in GS as a result of the synergistic effect in strain hardening [17]. Here, the change of KAM values at TBs and GBs shows the conclusive role in HDI strain hardening particularly in GL of low ductility. On one hand, the increase in $\overline{K}$ near TBs in GL is visible from 0.6° (before tensile deformation) to 1.0° (after), see two blue curves in lower panels in Fig. 4g and h, together with the simultaneous increase in the proportion of large KAM values. The closer observation is the larger KAM values near TB than those inside DTs, see Fig. 4i. These are the direct reflection for TBs acting as hetero-interfaces to induce the GNDs during plastic deformation. These GNDs are considered as the origin of HDI strain hardening [9–11]. In other words, these DTs exhibit sustainable strain hardening, although they are formed already during SMAT, together with the entangled dislocations of high-density (Fig. 2a). On the other hand, $\overline{K}$ near GBs increases from 0.8° (before tensile deformation) to 1.4° (after), see two blue curves in upper panels in Fig. 4g and h, also with the concurrent rise in the proportion of large KAM values. Even, the increment in $\overline{K}$ is a little bit larger near GBs (0.6°) than that near DTs (0.4°). This indicates the similar role by GBs in producing the GNDs. This is the reason of the presence of hysteresis loops (Fig. 3c) and of comparable residual plastic strains in both GS and standalone CG samples (Fig. 3d). In CG sample, different grains have different orientations and Schmid factors. That is to say, a part of grains have hard orientations and the left have soft ones. As a result, GBs in CG microstructure serve as hetero-interfaces where GNDs are produced during tensile deformation. These GNDs are exactly the origin of both HDI stress and corresponding HDI strain hardening as well in standalone CG samples. However, note that the much larger frequency of TBs than that of GBs, see Fig. 4j. It is argued that TBs in GL will play a role in HDI hardening larger than GBs do.

The strain hardening in GS is further depicted in terms of the increment of H_V as shown in Fig. 1b. Interestingly, a moderate increase in H_V (blue curve), i.e., an increment of H_V (red curve), appears in the top layer after tensile deformation. This is in sharp contrast to softening due to the mechanically driven growth of tiny nano-grains during tensile deformation [13]. Here, the increase in H_V is due mainly to the mechanically stable TBs [26]. Further, the GNDs near TBs interact with the gliding dislocations to effectively restrain TBs to migrate, usually as a softening mechanism during tensile deformation. By comparison, the CG shows a significant rise in H_V, indicating strong hardenability as a result of DTs, along with the conventional dislocation plasticity.

The strain hardening is further analyzed as a result of KAM evolution in CG layer of GS. Note that DTs of high density are formed during tensile deformation (Fig. 4f). $\overline{K}$ near TBs is 0.7°, see orange curve in lower panel, Fig. 4h. This value is less than that (1.0°) in GL, along with a less proportion of larger KAM values, lower panel in Fig. 4h. This indicates that TBs in CG layer contribute to less HDI stress than those in GL do. Further, $\overline{K}$ near GBs is 1.1° (see orange curve, upper panel in Fig. 4h), a little bit larger than $\overline{K}$ near TBs (0.7°). Yet, this does not necessarily mean the larger role by GBs than TBs. This is also due to the higher density of TBs than GBs. Here TBs is again stressed for HDI hardening. Finally, it is visible that the increment in $\overline{K}$ of 0.4° near TBs in GL is less than that of 0.7° in CG layer. This is due to twinning to happen in large CG grains within a large range of plastic strain. This is probably the reason that three values, i.e., ε_{rp} (Fig. 3d), $\sigma_{HDI}/\sigma_{flow}$, and $\Theta_{HDI}/\Theta_{flow}$ (upper and lower panels in Fig. 3e), all show the similar trend: they become larger in CG than those in GS during the later stage of tensile deformation.

5. Conclusions

In the present study, the deformation twin-density gradient structure was fabricated in an S31254 SASS by using the SMAT technology. Both tensile properties as well as associated microstructural evolutions were investigated, with the emphasis on the mechanism of strain hardening. The main conclusions were drawn in the following.

(1) The GS consists of two gradient layers sandwiching the centered coarse-grained core. In the gradient layer, the density of nano-scale DTs appears gradient.
(2) Yield strength in GS has doubled to 0.5 GPa as compared to that in coarse-grained counterpart, along with comparable ductility of 36%. The trade-off in strength and ductility is largely alleviated in GS. The persistent presence of hysteresis loops during unload-and-reload tensile deformation shows that both HDI stress and HDI strain hardening account for, respectively, a large proportion of flow stress and global strain hardening.

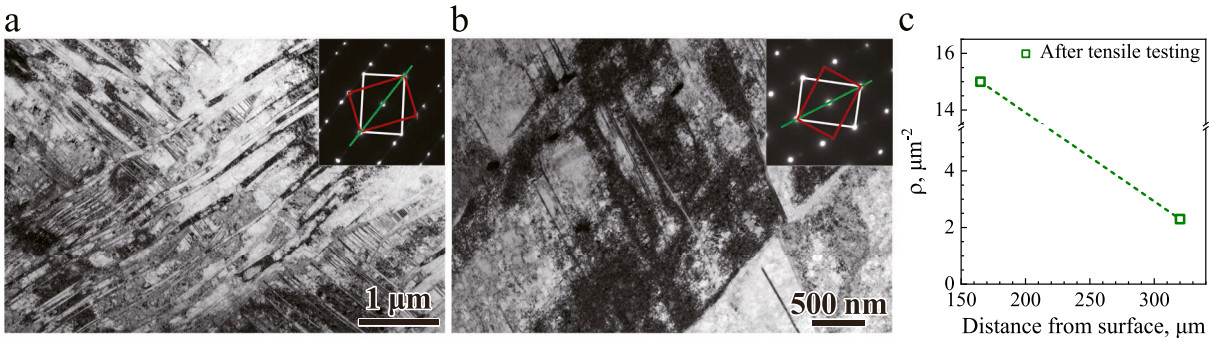

Fig. 5. TEM images of GS after tensile testing. (a)–(b) Bright field images at depth of ~170 and 330 μm depth from the surface, respectively. Inset in each map: the corresponding selected area electron diffraction (SAED) pattern of twin, all with the [011] zone axis. (c) Statistical density of nanotwins at different depth after tensile testing.

(3) An obviously increased kernel misorientation values are noted near the twin boundaries of high density as a result of the formation of the geometrically-necessary dislocations. Deformation twins, already produced during previous plastic deformation, are capable of further strain hardening. Twin boundaries can serve as the origin for HDI hardening for the enhanced strength-ductility combination at an elevated yield strength. TBs contribute more to strain hardening than grain boundaries in the GS.

CRediT authorship contribution statement

Ting-Ting Chen: Investigation, Visualization, Writing - Original Draft.**Jing Wang:**Investigation, Validation.**Yi Zhang:** Investigation. **Ping Jiang:** Validation. **Fu-Ping Yuan:** Investigation, Validation. **Pei-De Han:**Conceptualization, Resources, Funding acquisition, Supervision. **Xiao-Lei Wu:**Conceptualization, Validation, Writing - Review & Editing, Funding acquisition, Supervision.

Declaration of competing interest

The authors declare that they have no known competing financial interests or personal relationships that could have appeared to influence the work reported in this paper.

Acknowledgement

This work was supported by the Ministry of Science and Technology of China (Grant Nos. 2019YFA0209900 and 2017YFA0204402), NSFC Basic Science Center Program (Grant Nos. 11988102), NSFC (Grant Nos. 51871159, 11972350, and 11890680) and the Chinese Academy of Sciences (Grant No. XDB22040503).

References

[1] Y.T. Zhu, X.L. Wu, Ductility and plasticity of nanostructured metals: differences and issues, Mater, Today Nano 2 (2018) 15–20.
[2] K. Lu, Stabilizing nanostructures in metals using grain and twin boundary architectures, Nat. Rev. Mater. 1 (2016) 16019.
[3] R.Z. Valiev, I.V. Alexandrov, Y.T. Zhu, T.C. Lowe, Paradox of strength and ductility in metals processed by severe plastic deformation, J. Mater. Res. 17 (2002) 5–8.
[4] Y.M. Wang, M.W. Chen, F.H. Zhou, E. Ma, High tensile ductility in a nanostructured metal, Nature 419 (2002) 912–915.
[5] Y.T. Zhu, X.Z. Liao, Nanostructured metals: retaining ductility, Nat. Mater. 3 (2004) 351–352.
[6] Y.M. Wang, E. Ma, Three strategies to achieve uniform tensile deformation in a nanostructured metal, Acta Mater. 52 (2004) 1699–1709.
[7] R.Z. Valiev, R.K. Islamgaliev, I.V. Alexandrov, Bulk nanostructured materials from severe plastic deformation, Prog. Mater. Sci. 45 (2000) 103–189.
[8] Y.F. Liu, Y. Cao, Q.Z. Mao, H. Zhou, Y.H. Zhao, W. Jiang, Y. Liu, J.T. Wang, Z. S. You, Y.T. Zhu, Critical microstructures and defects in heterostructured materials and their effects on mechanical properties, Acta Mater. 189 (2020) 129–144.
[9] Y.T. Zhu, K. Ameyama, P.M. Anderson, I.J. Beyerlein, H.J. Gao, H.S. Kim, E. Lavernia, S. Mathaudhu, H. Mughrabi, R.O. Ritchie, N. Tsuji, X.Y. Zhang, X. L. Wu, Heterostructured materials: superior properties from hetero-zone interaction, Mater. Res. Lett. 9 (2021) 1–31.
[10] Y.F. Wang, M.S. Wang, X.T. Fang, F.J. Guo, H.Q. Liu, R.O. Scattergood, C.X. Huang, Y.T. Zhu, Extra strengthening in a coarse/ultrafine grained laminate: role of gradient interfaces, Int. J. Plast. 123 (2019) 196–207.
[11] E. Ma, T. Zhu, Towards strength–ductility synergy through the design of heterogeneous nanostructures in metals, Mater. Today 20 (2017) 323–331.
[12] H. Zhou, C.X. Huang, X.C. Sha, L.R. Xiao, X.L. Ma, H.W. Höppel, M. Göken, X. L. Wu, K. Ameyama, X.D. Han, Y.T. Zhu, In-situ observation of dislocation dynamics near heterostructured interfaces, Mater. Res. Lett. 7 (2019) 376–382.
[13] T.H. Fang, W.L. Li, N.R. Tao, K. Lu, Revealing extraordinary intrinsic tensile plasticity in gradient nano-grained copper, Science 331 (2011) 1587–1590.
[14] X.L. Wu, P. Jiang, L. Chen, F.P. Yuan, Y.T. Zhu, Extraordinary strain hardening by gradient structure, Proc. Natl. Acad. Sci. U.S.A. 111 (2014) 7197–7201.
[15] M.X. Yang, D.S. Yan, F.P. Yuan, P. Jiang, E. Ma, X.L. Wu, Dynamically reinforced heterogeneous grain structure prolongs ductility in a medium-entropy alloy with gigapascal yield strength, Proc. Natl. Acad. Sci. U.S.A. 115 (2018) 7224–7229.
[16] S.K. Vajpai, M. Ota, Z. Zhang, K. Ameyama, Three-dimensionally gradient harmonic structure design: an integrated approach for high performance structural materials, Mater. Res. Lett. 4 (2016) 191–197.
[17] X.Y. Li, L. Lu, J.G. Li, X. Zhang, H.J. Gao, Mechanical properties and deformation mechanisms of gradient nanostructured metals and alloys, Nat. Rev. Mater. 5 (2020) 706–723.
[18] K. Lu, Making strong nanomaterials ductile with gradients, Science 345 (2014) 1455–1456.
[19] M.X. Yang, Y. Pan, F.P. Yuan, Y.T. Zhu, X.L. Wu, Back stress strengthening and strain hardening in gradient structure, Mater. Res. Lett. 4 (2016) 145–151.
[20] Y.F. Wang, C.X. Huang, M.S. Wang, Y.S. Li, Y.T. Zhu, Quantifying the synergetic strengthening in gradient material, Scripta Mater. 150 (2018) 22–25.
[21] Z. Cheng, H.F. Zhou, Q.H. Lu, H.J. Gao, L. Lu, Extra strengthening and work hardening in gradient nanotwinned metals, Science 362 (2018) 559.
[22] Z. Cheng, L. Lu, The effect of gradient order on mechanical behaviors of gradient nanotwinned Cu, Scripta Mater. 164 (2019) 130–134.
[23] T. Wan, Z. Cheng, L.F. Bu, L. Lu, Work hardening discrepancy designing to strengthening gradient nanotwinned Cu, Scripta Mater. 201 (2021) 113975.
[24] K.Y. Zhu, A. Vassel, F. Brisset, K. Lu, J. Lu, Nanostructure formation mechanism of α-titanium using SMAT, Acta Mater. 52 (2004) 4101–4110.
[25] J.S. Li, W.D. Gao, Y. Cao, Z.W. Huang, B. Gao, Q.Z. Mao, Y.S. Li, Microstructures and mechanical properties of a gradient nanostructured 316L stainless steel processed by rotationally accelerated shot peening, Adv. Eng. Mater. 20 (2018) 1800402.
[26] H.T. Wang, N.R. Tao, K. Lu, Architectured surface layer with a gradient nanotwinned structure in a Fe–Mn austenitic steel, Scripta Mater. 68 (2013) 22–27.
[27] J.J. Wang, N.R. Tao, K. Lu, Revealing the deformation mechanisms of nanograins in gradient nanostructured Cu and CuAl alloys under tension, Acta Mater. 180 (2019) 231–242.
[28] K. Lu, J. Lu, Nanostructured surface layer on metallic materials induced by surface mechanical attrition treatment, Mater. Sci. Eng. A 375–377 (2004) 38–45.
[29] X.C. Liu, H.W. Zhang, K. Lu, Strain-induced ultrahard and ultrastable nanolaminated structure in nickel, Science 342 (2013) 337–340.
[30] D.A. Hughes, N. Hansen, Graded nanostructures produced by sliding and exhibiting universal behavior, Phys. Rev. Lett. 87 (2001) 135503.
[31] X. Wang, Y.S. Li, Q. Zhang, Y.H. Zhao, Y.T. Zhu, Gradient structured copper by rotationally accelerated shot peening, J. Mater. Sci. Technol. 33 (2017) 758–761.
[32] C.C. Wu, S.H. Wang, C.Y. Chen, J.R. Yang, P.K. Chou, J. Fang, Inverse effect of strain rate on mechanical behavior and phase transformation of superaustenitic stainless steel, Scripta Mater. 56 (2007) 717–720.
[33] E.A. Abd Ei Meguid, A.A. Abd Ei Latif, Critical pitting temperature for type 254 SMO stainless steel in chloride solutions, Corros. Sci. 49 (2007) 263–275.
[34] H. Gao, Y. Huang, W.D. Nix, J.W. Hutchinson, Mechanism based strain gradient plasticity—I, Theory, J. Mech. Phys. Solids 47 (1999) 1239–1263.
[35] I. Gutierrez-Urrutia, F. Archie, D. Raabe, F. Yan, N. Tao, K. Lu, Plastic accommodation at homophase interfaces between nanotwinned and recrystallized grains in an austenitic duplex-microstructured steel, Sci. Technol. Adv. Mater. 17 (2016) 29–36.
[36] D.D. Zhang, J.Y. Zhang, J. Kuang, G. Liu, J. Sun, Superior strength-ductility synergy and strain hardenability of Al/Ta co-doped NiCoCr twinned medium entropy alloy for cryogenic applications, Acta Mater. 220 (2021) 117288.
[37] H.H. Zhi, C. Zhang, S. Antonova, H.Y. Yu, T. Guo, Y.J. Su, Investigations of dislocation-type evolution and strain hardening during mechanical twinning in Fe-22Mn-0.6C twinning-induced plasticity steel, Acta Mater. 195 (2020) 371–382.